Engineering Structures 195 (2019) 309–323

Contents lists available at ScienceDirect

Engineering Structures

journal homepage: www.elsevier.com/locate/engstruct

Experimental study on the seismic performance of round-ended hollow piers

Changjiang Shao[a,b,*], Qiming Qi[a], Meng Wang[a], Zhenghao Xiao[a], Wang Wei[a], Chenxu Hu[a], Laichuan Xiao[a]

[a] Civil Engineering School of Southwest Jiaotong University, Chengdu 610031, China
[b] National Engineering Laboratory for Disaster Prevention Technology in Land Transportation, Chengdu 610031, China

ARTICLE INFO

Keywords:
Round-ended hollow piers
Damage behavior
Plastic hinge
Displacement ductility
Seismic performance objective
Cyclic test

ABSTRACT

To investigate the seismic performance of railway bridge piers with round-ended hollow section, five 1/6-scale specimens were tested under low-cyclic loading. The two variable parameters were the volumetric stirrup ratio and axial load level. The damage evolution, strain response, and plastic hinge behavior were meticulously explored. The load-drift relationship, displacement ductility, strength/stiffness degradation, dissipated energy, and viscous damping were analyzed in depth. The quantification of seismic performance objectives was implemented by displacement ductility based on damage assessment. The relationships among the ductility and strength/stiffness degradation and equivalent damping ratio were regressed using the test data. The experiment and analysis results showed that all specimens suffered flexural failure, with flexural cracks covering nearly two-thirds of the pier height. The plastic hinge region lengthened and moved upwards along the column due to the existence of solid segment, internal chamfer and variable section. The displacement ductility capacity enhanced noticeably with increasing stirrup ratio. The increasing axial compression ratio led to higher initial stiffness and seismic capacity to some extent, but excessive axial load would decrease ductility with premature concrete crushing. Furthermore, the seismic safety of the piers were ensured under a ductility factor limitation of 4.8 required by the current seismic code for railway engineering of China.

1. Introduction

With the robust expansion of high-speed rail (HSR) network in recent years, a large number of standard short-span bridges (including simply supported beam bridges and a few continuous beam bridges) have been constructed or are being built in the southwest region of China [1,2]. To accommodate the rugged topography of mountainous areas, the height of these piers is usually over 30 m [3]. For slender railway bridge columns, the round-ended hollow piers are usually selected as the substructure [4], which not only saves material, lowers self-weight and reduces seismic inertial forces compared with traditional solid piers, but also meets with the stiffness requirement for HSR bridges. However, the Southwest China is known for frequent intensive earthquakes (such as the Wenchuan Earthquake in 2008 and the Lushan Earthquake in 2013). The railway bridges with thin-walled slender columns are vulnerable to seismic damage, so their seismic performance need to be studied in depth.

To date, numerous experiments have been finished on rectangular (e.g., [5–10]) and circular (e.g., [11,12]) hollow columns. Mander et al. [5] concentrated on the seismic performance of rectangular hollow columns via semi-static tests of four reduce-scaled models. A series of experiments on full or reduce-scaled rectangular hollow columns were conducted by Yeh and Mo [6–8] since 2000. Furthermore, biaxial quasi-static tests were also performed on rectangular hollow pier specimens [9,10]. For circular hollow piers, Zahn [11] and Yeh [12] studied the flexural strength and ductility behavior respectively.

Generally, the above research strongly promoted experimental methods and analytical theory for hollow columns. However, great discrepancies may exist among rectangular, circular and round-ended hollow columns subjected to earthquake impacts. Because section type, reinforcement details and concrete confinement of these members are greatly different. Although several experiments were implemented on round-ended hollow piers [13,14], the reduce-scaled specimens were usually simplified by uniform hollow section without solid segment and internal chamfer at the pier base. As a result, the damage mechanism and plastic hinge behavior of the actual round-ended hollow piers might greatly differ from the test results of the existing experiments [5–14]. Meanwhile, the performance such as hysteresis behavior, strength/stiffness, energy dissipation, and viscous damping may also be different with previous research. Additionally, the current seismic design code of railway engineering of China [15] did not offer any specific seismic design methods for hollow piers. Till now, there haven't been

* Corresponding author at: Civil Engineering School of Southwest Jiaotong University, Chengdu 610031, China.

https://doi.org/10.1016/j.engstruct.2019.05.094
Received 6 October 2018; Received in revised form 26 May 2019; Accepted 28 May 2019

any experimental investigations on how and to what extent solid segment, internal chamfer and variable section would exert effects on the seismic performance for hollow columns. Therefore, experiments should be conducted to find out the damage mechanism and seismic performance for this kind of hollow members.

This paper mainly comprises four parts, in addition to the introduction. First, five 1/6-scale round-ended hollow specimens were designed according to the current seismic code for railway engineering [15], with stirrup ratio and axial load level being the design parameters. Some details of the specimens and the experimental phenomena were described. Second, the damage behavior, evolution mechanism of plastic hinge as well as the strain response were explored. In the discussion on the test results, the seismic performance was evaluated in terms of hysteretic performance, displacement ductility, strength/stiffness, dissipated energy, and damping ratio. Quantification for seismic performance objectives was implemented using displacement ductility combined with damage assessment. The performance objectives were associated with strength/stiffness degradation. A model of equivalent damping ratio is proposed through regression on the test data. Finally, some instructive conclusions were obtained to help understand the flexural performance of a round-ended hollow-section pier under seismic loading.

2. Experimental program

2.1. Specimen design and material properties

Simply supported railway bridges and standard continuous beam bridges with round-ended section piers are extensively popular in China for their adaptability to all kinds of landforms. The round-ended hollow section is usually adopted when the pier height exceeded 30 m. In this study, a kind of multispan simply supported railway bridge with a uniform span of 32 m was chosen as the prototype, and a single pier of 30 m was selected to design the test models under cyclic loading, as presented in Fig. 1.

The geometry and reinforcement details of the 1/6-scale pier models were illustrated in Fig. 2, with the elevation views and three-dimensional figure being included. The design height of the specimens was 5.0 m from the pier base to the centerline of the loading cap. Specifically, the solid segment and internal chamfer at pier base, along with variable hollow section, were included in the specimens (Fig. 2a). Unlike hollow piers studied previously with the same cross-section shape along the whole pier height [5–12], the slope of the outer wall of the test specimens was 40:1, and that of the inner wall was 70:1. The maximum sizes along the directions of the strong and weak axis were 0.825 m and 1.125 m at the bottom, respectively, while the minimum sizes were 0.60 m and 0.90 m at the neck of the pier. The stiffness of the hollow section increased from Section A to Section C, with a web thickness varying from 74 mm to 113 mm. As a result, the seismic damage mechanism of this kind of railway piers might differ from the members with uniform section.

The geometry and rebar arrangement of several sections (A, B, C, and D) were shown in Fig. 3, corresponding to the positions presented in Fig. 2a. Due to the changing section along the pier, Section C was chosen as the control section for the reinforcement design. The longitudinal reinforcement ratio (ρ_l) was 0.906% with 24 d = 12 mm rebars (Fig. 3c). The volumetric percentage of the stirrup (ρs) of the core concrete including transverse and tie reinforcement at the Section C varied from 0.325% to 1.510% for different specimens, with d = 6 mm plain bars spacing at distances of 60 mm, 100 mm, and 280 mm, respectively (Fig. 2a). In the middle part of the pier, the spaces enlarged to 90 mm, 150 mm, and 420 mm (Fig. 3b). The tie stirrups were arranged between the opposite longitudinal bars with 135° hooks to ensure the effectiveness of the confinement of the kernel concrete. The volumetric stirrup ratio (ρ_s) and axial compression ratio (η) were the key parameters in this experiment. The actual volumetric stirrup ratio of the prototype pier at the control section equaled to 0.971%, and the minimum stirrup ratio was 0.30% specified in the seismic code of China [15]. Therefore, the ratios designed in this experiment could be used to investigate the influence of stirrup on the seismic performance of round-ended hollow piers. The axial compressive ratio in railway engineering practice ranged from 0.04 to 0.10 [14], thus the ratios at Section C were 0.10, 0.15, and 0.20, considering the variation of axial load under strong earthquake. The main design parameters of specimens were summarized in Table 1.

As for the material properties, the average compressive strength (f_c') ranged from 32.0 to 34.7 MPa obtained from 15 × 15 × 15 cm^3 cubic samples. The actual yielding and ultimate strength of the longitudinal rebars were, on average, 445 MPa and 587 MPa, while those of the stirrups were 349 MPa and 516 MPa respectively.

2.2. Loading setup

The loading setup, located in the National Engineering Laboratory for Disaster Prevention Technology in Land Transportation (NEDL) (Southwest Jiaotong University), was shown in Fig. 4. All the tests were conducted in the reaction-frame loading system with constant vertical compressive load and cyclic lateral load. The constant vertical compression on the top of each specimen was applied by a 3000 kN hydraulic jack. The lateral loading was exerted by a 1000 kN MTS actuator. The specimens were loaded along the E-W direction (the side facing the reaction wall was the E side, while that facing away from the wall was the W side).

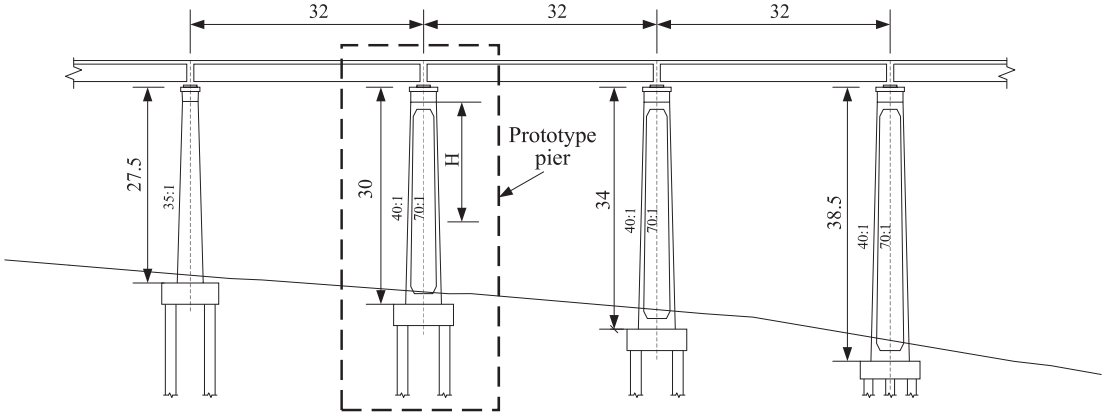

Fig. 1. Prototype of a multispan simply supported bridge (unit: m).

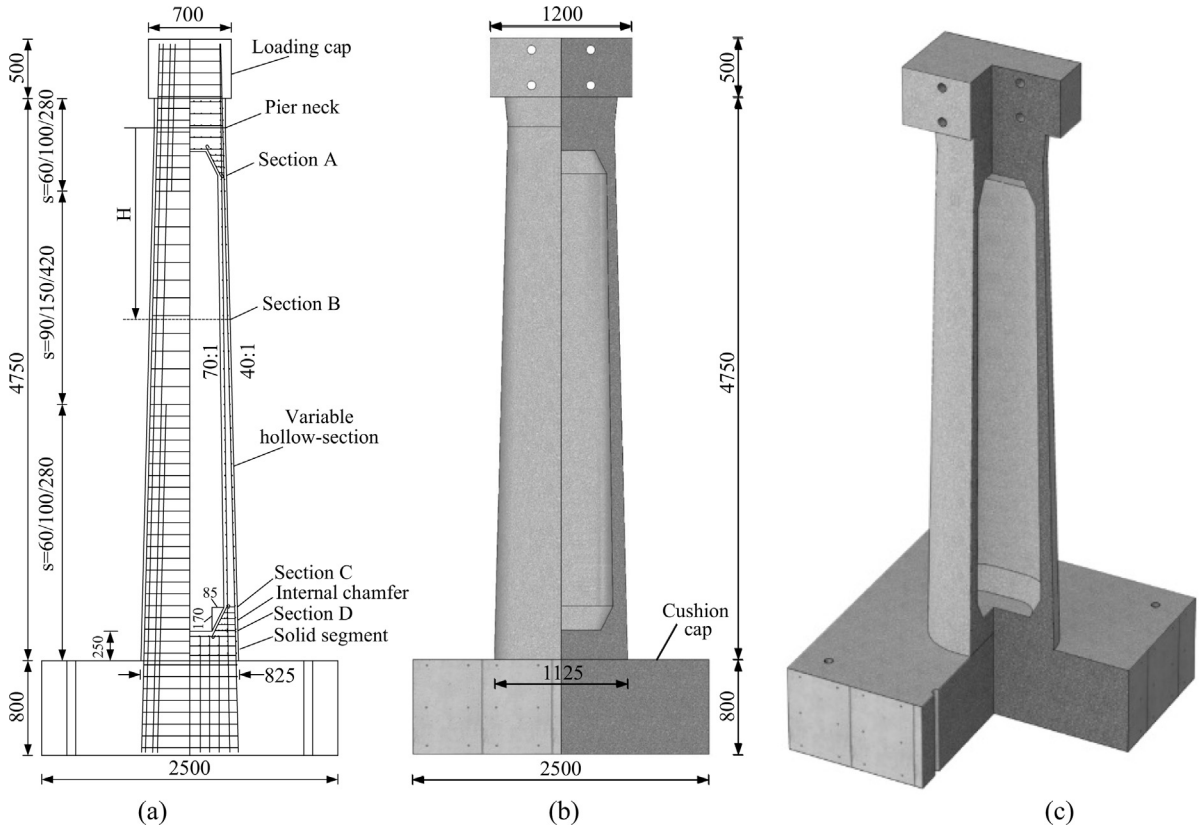

Fig. 2. Details of the test specimen: (a) rebar arrangement in side view; (b) front view; and (c) 3D graph (unit: mm).

2.3. Test instrument

The main parameters measured included displacement, loading force and strain. During the loading process, the damage evolution was carefully observed and recorded, and the test data were documented by the acquisition system. The horizontal displacement was acquired by the laser displacement sensors placed at height of 0.4 m, 0.8 m, 1.2 m, 2.8 m and the centerline of the top cap. The wire-type displacement transducers were arranged vertically on the E and W sides to measure average curvature within the potential plastic region of a pier [16] (seen in Fig. 4). In addition, four linear variable differential transformers (LVDTs) were installed perpendicularly to the front face to capture the possible sliding of a cushion cap. Two LVDTs were vertically fixed to the top face of the cap to measure the possible rotation of the pier.

The arrangement of the strain gauges in each cross-section was shown in Fig. 5a. Three groups of strain gauges were used on steels, namely, 40 gauges for longitudinal reinforcement, 20 for the transverse bar and 15 for the tie bar. These strain gauges were placed at the height of 20 cm, 42 cm, 75 cm, 410 cm and 430 cm along the pier. The concrete strain gauges were attached along the loading direction (E&W) and the side faces (N&S) within the region of potential plastic hinge (Fig. 5d and e). During the test process, the data of strain, displacement, and loading force were acquired by the MTS AeroPro acquisition system.

2.4. Loading protocol

The cyclic loading protocol was shown in Fig. 6. The amplitudes were expressed in both displacement Δ and corresponding drift which was the ratio of Δ to pier height. At the beginning of the test, an initial axial loading was applied to verify that there was no obvious eccentricity. A small lateral loading (20 kN) was applied in both push and pull cycle to check the stability of the test system. Then, the target axial compression was applied. Initially, the lateral load was applied by force-control mode determined from FEA modeling to get the initial cracking of the pier. Subsequently, the displacement-control mode was adopted, namely, imposed displacement cycles were repeated twice with the increasing amplitudes of Δ_{yi}, $2.0\Delta_{yi}$, $3.0\Delta_{yi}$, $4.0\Delta_{yi}$ … until failure. Δ_{yi} was determined by the FEA simulation, which was 24 mm (0.48%), 29 mm (0.58%), 25 mm (0.50%) and 26 mm (0.52%) for SA1, SA2, SA3, SB1, and SB2, respectively. The test was terminated when the lateral capacity dropped to 85% of the previous maximum force [17].

3. Experimental observation

3.1. Damage description

It was found that all specimens suffered flexure-type failures. The damage evolution of each specimen was attentively observed and recorded with the increasing lateral load or displacement. The five specimens all experienced the course of incubation and extension of the flexural and diagonal cracks, initial spalling and final crushing of concrete. The plastic hinge formed as expected in all specimens, which finally led to the flexural failure of piers.

The damage characteristics of specimen SA1 could be seen in Fig. 7, which outlined the evolution of cracks on the west side and the final damage state on the other three sides. At the force-control stage, initial horizontal micro-cracks were firstly detected at the base when the lateral force was 110 kN and the corresponding displacement was approximately 8.5 mm (0.17%). When the lateral loading was up to 120 kN, as shown in Fig. 7a, the first visible flexural crack appeared at the height of around 0.42 m from the pier base, with a corresponding displacement of 12 mm (0.24%). Thus, the most unfavorable position was approximately at the upper edge of the internal chamfer (Section C in Fig. 3c).

At the displacement-controlled stage, three newborn cracks came

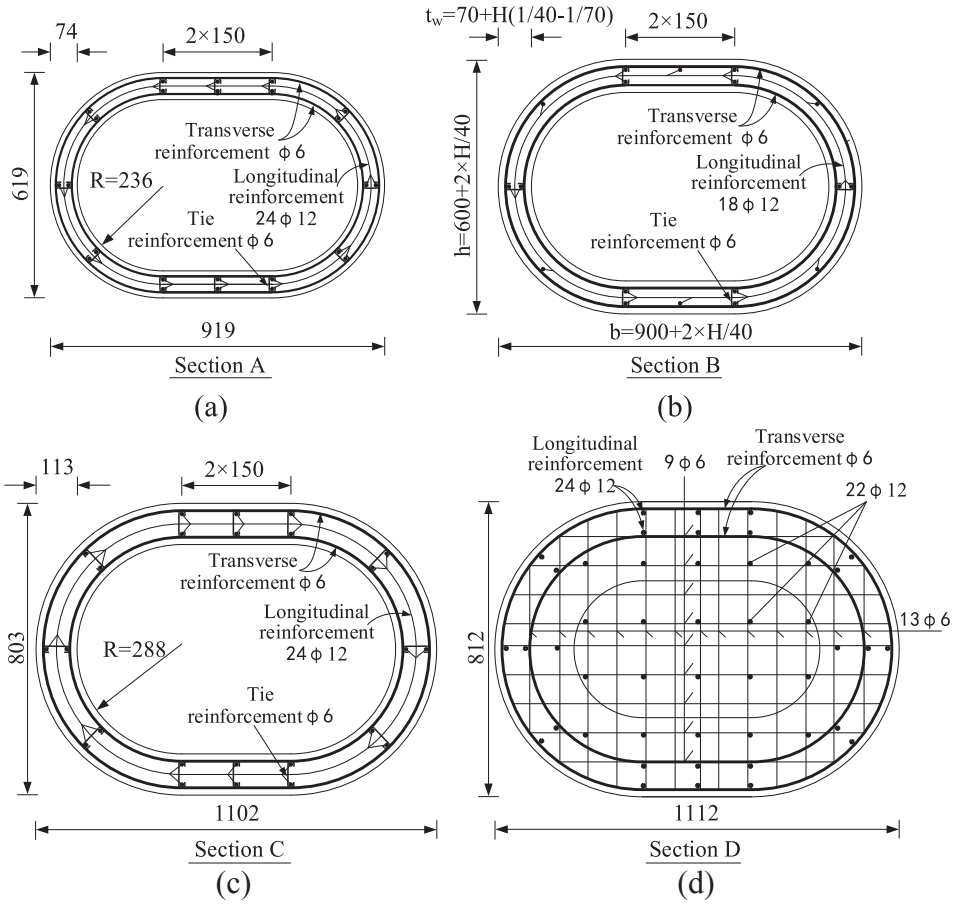

Fig. 3. Geometry and rebar arrangement of Section A (a), Section B (b), Section C (c), and Section D (d) (unit: mm).

into being on the E and W sides under the FEA-determined yielding displacement of 24 mm (0.48%), covering nearly one-third of the pier (seen in Fig. 7a). Exactly, the longitudinal steel yielded during the second pushing action at this drift level. The width of the existing cracks increased, and a large number of new flexural cracks came into being at a drift of 48 mm (0.96%), which indicated the preliminary formation of a plastic hinge. The distance between horizontal cracks was about 28 cm nearly equaling to the space between the adjacent transverse bars. Furthermore, some diagonal and vertical cracks formed on the N&S side faces and E&W front faces. As the drift equaled to 72 mm (1.44%), the evolution speed of the flexural cracks decreased, and some oblique cracks crossed each other. When the drift reached 96 mm (1.92%), the flexural cracks expanded deeply into the cross section, and the whole crack distribution covered almost two-thirds of the column. Besides, several vertical cracks came into being close to the bottom and the neck region due to the Poisson's effect. The lateral force reached the maximum value of 243.5 kN at this pushing load level. The concrete cover in the potential plastic-hinge region began to spall with a tip drift of 120 mm (2.40%). Meanwhile, the horizontal pulling load reached its maximum value of 239.3 kN. The subsequent inelastic cycles of 144 mm (2.88%) were characterized by widening flexural cracks and spalling concrete cover near the pier base. During the last cycle of the pushing load with a drift of 168 mm (3.36%), the concrete cover was completely spalled and crushed at the region close to the internal chamfer on the W side. As a result, the lateral load dropped sharply to 45.9% of the positive maximum value. In the condition of 3.36% drift ratio at pulling state, the lateral load decreased to 82.8% of the negative maximum force with tensile failure of the outmost rebar on the W side.

The failure processes of the other four specimens were similar to that of specimen SA1, but there were some differences in the damage behaviors due to different design parameters. The crack distribution along with damage evolution of the other four specimens could be seen in Fig. 8. The damage characteristics and the corresponding load or drift were listed in Table 2. A summary of the typical damage states was

Table 1
Main design parameters of the specimens.

Specimens	L (m)	L/D	η	Concrete	Longitudinal rebar		Stirrup rebar		
				f_c' (MPa)	ρ_l (%)	Layout	ρ_s (%)	d_s (mm)	s (mm)
SA1	5.0	6.06	0.15	32.0	0.906	24φ12	0.325	6	280
SA2	5.0	6.06	0.15	34.7	0.906	24φ12	0.910	6	100
SA3	5.0	6.06	0.15	32.0	0.906	24φ12	1.510	6	60
SB1	5.0	6.06	0.10	32.0	0.906	24φ12	0.910	6	100
SB2	5.0	6.06	0.20	33.4	0.906	24φ12	0.910	6	100

Note: The aspect ratio was defined as the quotient of the pier height (5 m) and maximum depth of round-ended cross section at the base along loading direction (0.825 m).

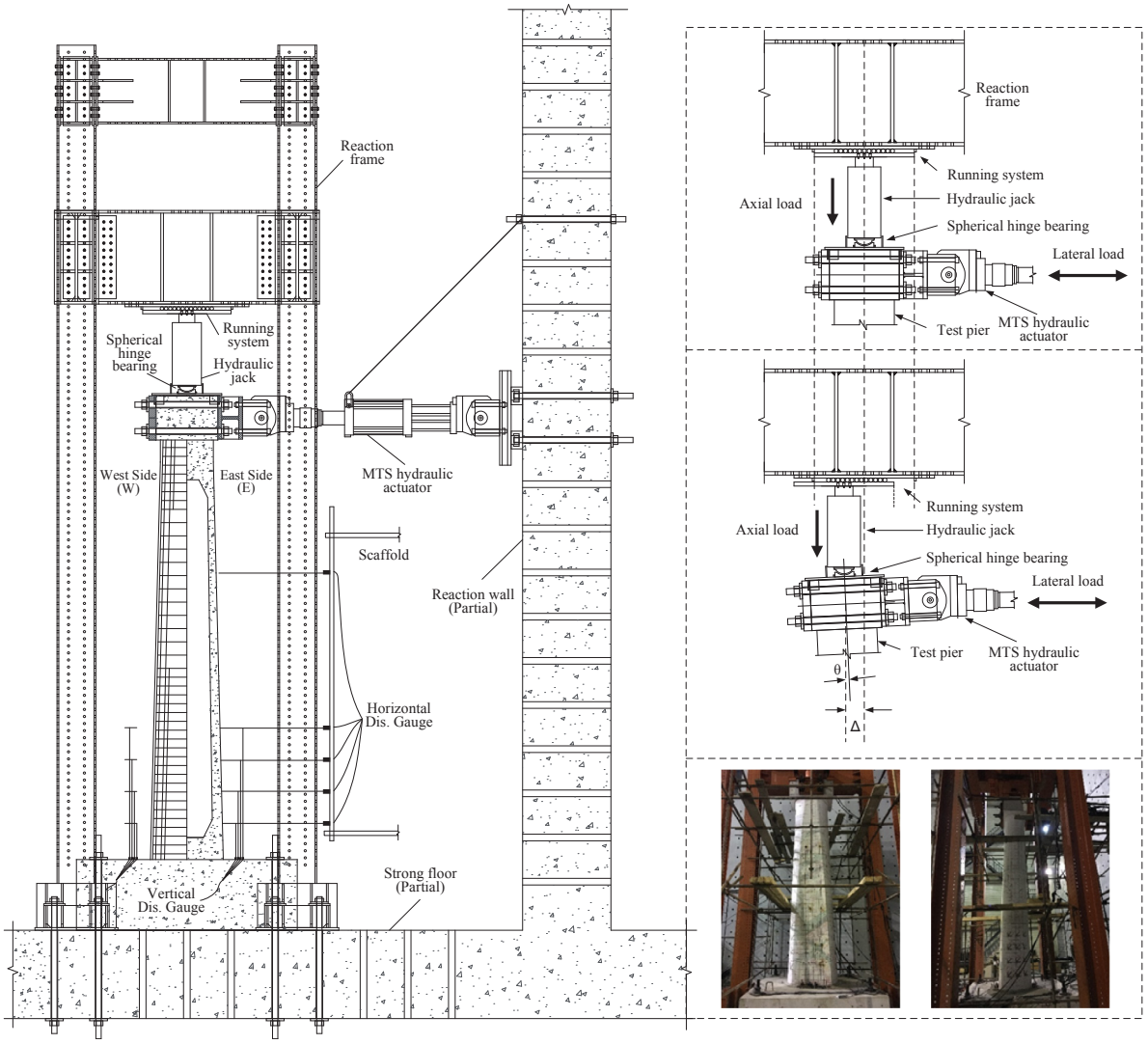

Fig. 4. Loading setup and layout of the test instruments.

listed in Table 3.

For specimen SB1 with compression ratio of 0.1, tiny cracks emerged close to the column bottom when the lateral force was only 50 kN. The first flexural crack of SB1 came into being under the action of 62 kN. Comparison among the specimens shows that the appearance of micro cracks was significantly influenced by the axial compression ratio. For all specimens, the drift ratio corresponding to the first yielding of the outermost longitudinal reinforcement was approximately 0.40–0.50%. It should be noticed that the yielding displacement in Table 2 was the actual drift corresponding to the yielding strain of

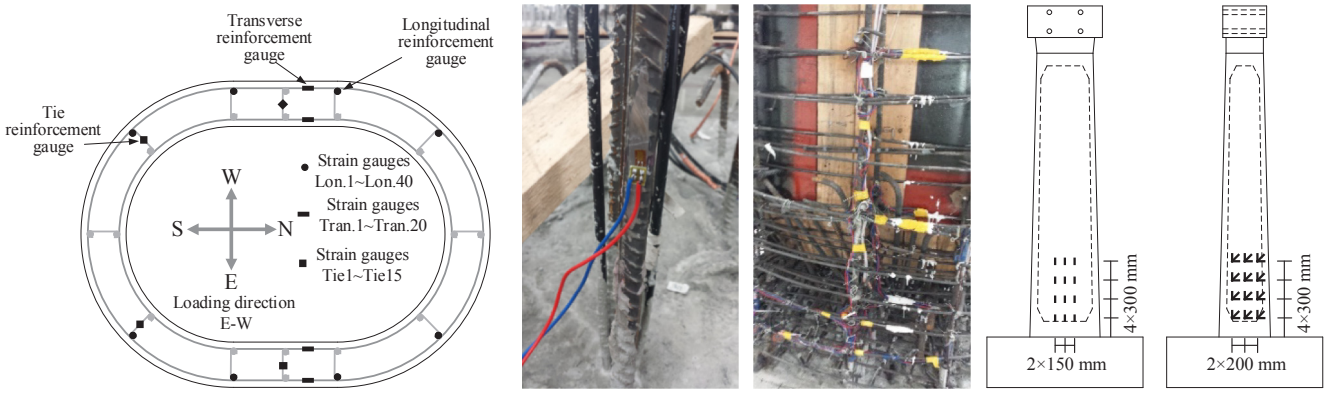

Fig. 5. Arrangement of strain gauges: (a) layout of rebar strain gauges; (b) strain gauge on longitudinal bar; (c) strain gauge on transverse bar; (d) concrete strain gauges on the E&W sides; (e) concrete strain gauges on the N&S sides.

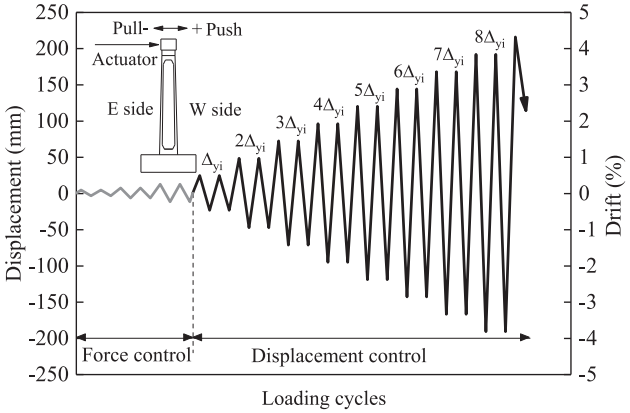

Fig. 6. Loading protocol.

the outermost longitudinal rebar, which was slightly smaller than the yielding shift based on simulation. The horizontal cracks sharply increased at the drift ratio of approximately 0.96–1.16%, and distributed nearly half of the pier. At the same time, some horizontal cracks began to extend obliquely to the side faces. The declined cracks mostly formed and crossed with the drift ratio from 1.44% to 2.0%, accompanied with some new cracks and continuous evolution of the existing cracks. Specifically, the declined cracks appeared and plastic regions formed initially at the largest drift ratio of 2.0% for SB1 compared with the other specimens. The drift ratio corresponding to the maximum load differed noticeably from 1.92% to 3.5% for the five columns, which mean increasing stirrup indicated the larger ultimate drift ratio. The lower ratio of axial compression mean a bigger drift of 3.50%. However, excessive compression would lead to premature failure due to concrete crushing of a pier. The example was the SB2 failed with a drift of only 2.06%, while the other specimens failed with a drift ratio of 3.36–4.06% because of crushing concrete cover and buckling/rupture longitudinal rebar. The final distribution of flexural cracks ranged from 61% to 75% of the pier height. The spacing of the horizontal cracks was regular which decreased with increasing stirrup ratio. The distribution of cracks was not symmetric due to the Baushengo's effect on the E and W sides. Although the aspect ratio of the specimens reached 6.06, noticeable inclined cracks appeared on the N and S sides, and irregular grids formed within one-third of the pier due to the interaction among axial load, moment, and shear force. However, there were almost no declined cracks in the round-ended solid piers even with a smaller aspect ratio [18], which indicated that the shear capacity of round-ended hollow piers was weaker than that of solid ones.

3.2. Strain response

Through strain analysis, the damage behavior of round-ended hollow pier could be further understood. The strains of steel and

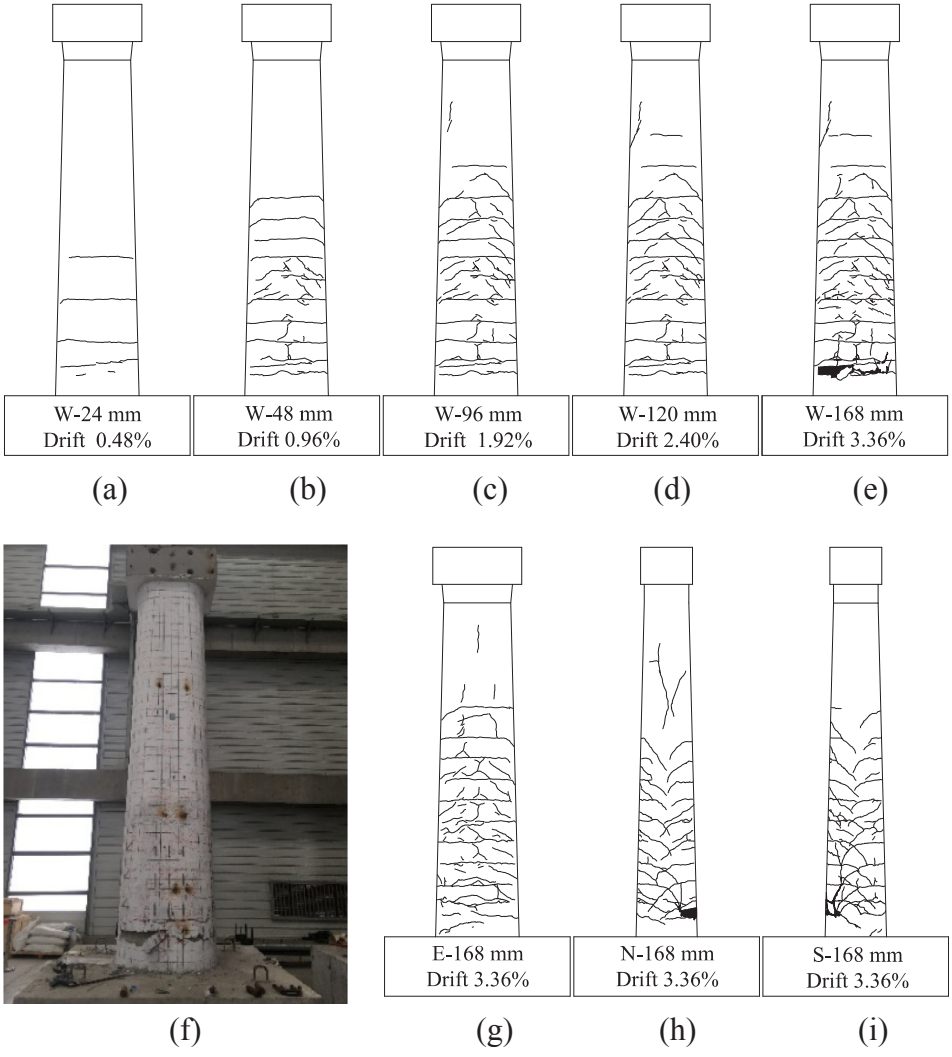

Fig. 7. Damage description of specimen SA1: damage evolution on the side W (a)–(e), and final damage state (f)–(i).

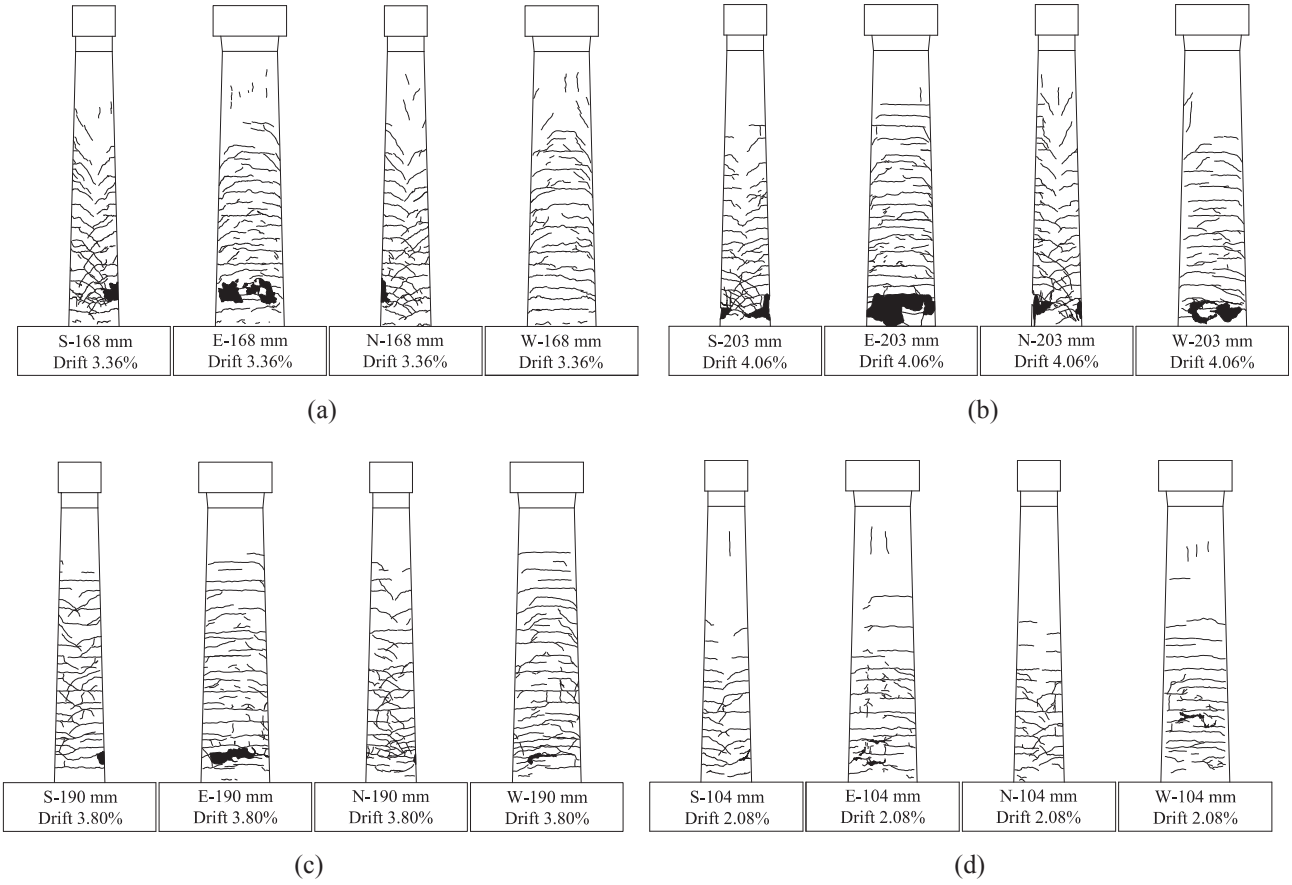

Fig. 8. Final damage description: (a) specimen SA2, (b) specimen SA3, (c) specimen SB1, and (d) specimen SB2.

concrete were shown in Fig. 9. The curves of longitudinal rebar strain versus the tip drift ratio at the heights of 0.20 m (solid segment), 0.42 m (at the upper edge of the internal chamfer) and 0.70 m respectively from the bottom of specimen SA1 could be seen in Fig. 9a. The strain-drift curve of gauge Lon. 1 was relatively plump when the region was under tensile state. The reason was that the force was mainly resisted by the longitudinal reinforcement after the concrete cover cracked, which resulted in a certain nonlinear residual strain when the horizontal drift was large enough. When it turned into compressive state, the concrete and longitudinal rebar were both under compression in the solid-section of piers, so the strain-drift curve was approximately linear. The maximum strain of Lon. 1 was near the yielding value (2225 με), then the yielding strain penetration was presumed to occur at the pier foundation [19]. Note that the strain gauge Lon. 9 was installed at the height of 0.42 m from the pier base, which yielded when the drift was only 22 mm (0.44%) and then the strain gauge failed. The strain-drift curve showed typical hysteretic characteristics and was almost symmetrical for the gauge Lon. 17. The strain value decreased after it reached the peak. The longitudinal strain also exhibited residual strain when pressed, possibly due to crushing of the web concrete or relative bond-slip between the steel and concrete.

The relationship between stirrup strain and drift of specimen SA1 was shown in Fig. 9b (at a height of 0.70 m). All the three gauges of stirrup at the same section were mostly tensile under pushing or pulling action due to the confinement effect of the kernel concrete. Since the compressive force (Tran. 9 and 10) was larger under pushing state than pulling stage. The strain of the outer transverse reinforcement (Tran. 9) was larger than that of the inner (Tran. 10).

The concrete strain on the E and S faces of specimen SA1 was shown in Fig. 9c. It could found that the maximum compressive strains of concrete (Con. 2, 8, and 20) corresponded to lateral drift of 24 mm (0.48%) with 1083 με, 741 με, and 689 με respectively. However, the strain turned abruptly to be tensile under the tip drift of 48 mm (0.96%) since concrete cracked. Finally, these three gauges failed due to too large width of cracks. The diagonal strain of concrete was demonstrated in Fig. 9c. It was noted that the shear strain of concrete was nearly invisible under the drift Δ_{yi}. When the tip drift reached $2\Delta_{yi}$, the diagonal cracks appeared. The stain of gauge Con. S8 increased to 7787 με at a drift of 46 mm (0.92%). That of gauge Con. S2 increased to 3745 με and 7365 με with a drift of 62 mm (1.24%) and 143 mm (2.86%) respectively. The shear strains of Con. S14 and S20 were relatively smaller than the others.

3.3. Behavior of plastic hinge

Although the plastic hinge behavior of solid piers has been studied extensively and numerous expressions have been proposed, the plastic properties of round-ended hollow piers were rarely investigated before. The average curvatures of specimen SA1, SA2, SA3 and SB1 (SB2 failed because of premature flexural failure) were drawn in Fig. 10, which increased with the increment of the tip drift ratio. It was interesting that the biggest average curvature ϕ_2 occurred close to the internal chamfer (region between 0.40 m and 0.80 m from the pier base), which was calculated using strain of longitudinal rebar and concrete shown in Fig. 9. However, there were often with lumped rotation at the bottom of either solid or hollow piers studied previously [5–10]. This phenomenon might attribute to the abrupt change of section between the solid segment and hollow part with internal chamfer being included at the base. As a result, the plastic region of the specimens were mainly formed around the upper edge of the internal chamfer (seen in Figs. 7 and 8). Under the final level of drift, the largest average curvature values of ϕ_2 were 0.062, 0.061, 0.074, and 0.072 for specimen SA1,

Table 2
Summary of the damage evolution.

Stage	Damage description	Force or displacement (Drift)				
		SA1	SA2	SA3	SB1	SB2
1	Incubation of hairline cracks	110 kN	100 kN	95 kN	50 kN	75 kN
2	First visible flexural cracks	120 kN	142 kN	120 kN	62 kN	110 kN
3	First yielding of the outermost longitudinal steel bar, with flexural cracks covering nearly one-third of the pier	22 mm (0.44%)	23 mm (0.46%)	25 mm (0.50%)	20 mm (0.40%)	20 mm (0.40%)
4	Surge evolution of the flexural cracks, and occurrence of some diagonal cracks	48 mm (0.96%)	48 mm (0.96%)	58 mm (1.16%)	50 mm (1.00%)	52 mm (1.04%)
5	Widening of flexural cracks, and declined cracks cross to form crack grids	72 mm (1.44%)	72 mm (1.44%)	87 mm (1.74%)	100 mm (2.00%)	78 mm (1.56%)
6	Maximum lateral load	+96 mm (1.92%)/−120 mm (2.40%)	± 120 mm (2.40%)	± 145 mm (2.90%)	± 175 mm (3.50%)	–
7	Failure due to concrete cover crushing and buckling/rupture of longitudinal rebar	168 mm (3.36%)	168 mm (3.36%)	203 mm (4.06%)	190 mm (3.80%)	104 mm (2.08%)

SA2, SA3, and SB1, respectively. The deformation in the plastic hinge region was quite different from the solid members. As shown in Fig. 11, the plastic rotation concentrated mainly on the chamfer and the nearby hollow-section segment, which was verified by damage observation, curvature distribution and strain response. In this study, the plastic hinge region moved upwards and lengthened slightly compared with the foregoing research [14].

4. Analysis on test results

4.1. Hysteretic response

The load-displacement (drift) hysteresis loops of the specimens were drawn in Fig. 12. It could be seen that the lateral load-drift curve was nearly linear at the initial stage of loading, which indicated the elastic state of the pier. With an increase in drift, the hysteresis loops became increasingly plump due to cracking and spalling of concrete cover as well as the slippage between concrete and longitudinal rebar. In each loading cycle, a slight reduction in strength and stiffness appeared at the second repeated loading step because of cumulative damage, which was much obvious in the loading cycles near the ultimate state. Finally, the lateral load of all specimens except for SB1 decreased sharply due to the severe crushing of concrete and buckling or rupture of the longitudinal rebar, with the remained capacity being 45.9%, 44.1%, 27.9% and 69.8% of the maximum force for SA1, SA2, SA3 and SB2, respectively. The pinching effect was more obvious in the loops of specimen SB1 than in those of the other four specimens. The hysteresis loops were plumper with more stirrup, possibly because of well confinement effect which played a significant role in the formation of a plastic hinge. Noted that the hysteresis curves were not strictly symmetric for specimens, especially for SA3 and SB1. It was due to the asymmetric damage accumulation under cyclic loading. The construction error for complicated geometric details of specimens might also be reason to cause the above unsymmetry.

4.2. Skeleton curve and ductility

The comparison of skeleton curves obtained from the hysteresis loops was shown in Fig. 13. The ductility factor (μ) was defined as the ratio of the ultimate displacement (Δ_u) to the corresponding yielding displacement (Δ_y). The ultimate displacement (Δ_u) was that corresponding to 85% of the lateral peak force [14]. However, there was divergence of the interpretation of the definition of yielding displacement (Δ_y) for various authors. In this study, two types of yielding displacement were defined such as the initial yield displacement (Δ_{yi}) and equivalent yielding displacement (Δ_{ye}). Δ_{yi} was the displacement corresponding to the first yielding of the outmost layer of longitudinal rebar in piers. While the definition of equivalent yielding displacement (Δ_{ye}) was proposed by Park [20] based on the energy equivalent method according to the skeleton curve. The displacements with the corresponding forces on the characteristic points and the ductility factors in terms of μ_{Park} and μ_{Ini} were listed in Table 4. The ductility factor μ_{Park} of specimens, except for SB2, ranged from 2.7 to 4.5 at ultimate state, while the factor μ_{Ini} ranges from 7.0 to 9.3. It was interesting to find that the values of μ_{Park} were almost twice those of μ_{Ini} for the specimens in this paper.

4.3. Degradation of strength and stiffness

Apart from the damage state and displacement ductility, strength and stiffness were also often employed to evaluate the seismic performance. Ductile RC members were designed to allow seismic damage with corresponding degradation in strength and stiffness. To investigate the rule of strength degradation of each specimen, a factor was put forward as follows:

Table 3
Summary of the pier damage.

Test specimen	Crack distribution (L_{cr}/L)		Concrete crushing		Vertical crack at the pier neck		Rebar buckling or fracture	
	E	W	E	W	E	W	E	W
SA1	0.62	0.70	–	✓	✓	✓	–	☑
SA2	0.67	0.64	✓	–	✓	✓	☑	–
SA3	0.72	0.62	✓	✓	✓	✓	☑	☑
SB1	0.75	0.75	✓	✓	–	–	☑	✓
SB2	0.61	0.67	✓	✓	✓	✓	✓	✓

Note: L_{cr} was the extent of crack distribution, ✓ indicated that the longitudinal rebar was only buckling, ☑ represented that the longitudinal rebar ruptured after buckling, and – meant none phenomena being recorded.

$$\gamma_i = \frac{V_i}{V_m} \tag{1}$$

where γ_i is the degradation factor of strength of the ith loading cycle, V_i is the peak strength of ith loading cycle, and V_m is the maximum strength of the loading course. The curves of strength degradation factor of the specimens were shown in Fig. 14.

The lateral demand increased with increasing ductility in an appropriate range, followed with a stable state before degradation. On the other hand, the lateral load bearing capacity often increasingly decreased due to reverse repeat actions. Through the comparison of strength deterioration curves, it showed that excellent ductility with no obvious strength deterioration of specimen SA3, which indicated the importance of confining stirrup. However, excessive axial compression would accelerate the failure of pier such as SB2.

The secant stiffness (K) in this study was defined as the ratio of the peak load to the corresponding displacement in each loading cycle. To evaluate the deterioration of stiffness of each specimen, a factor was defined as:

$$\lambda_i = \frac{K_i}{K_0} \tag{2}$$

where λ_i is the degradation factor of stiffness in the ith loading cycle, K_i

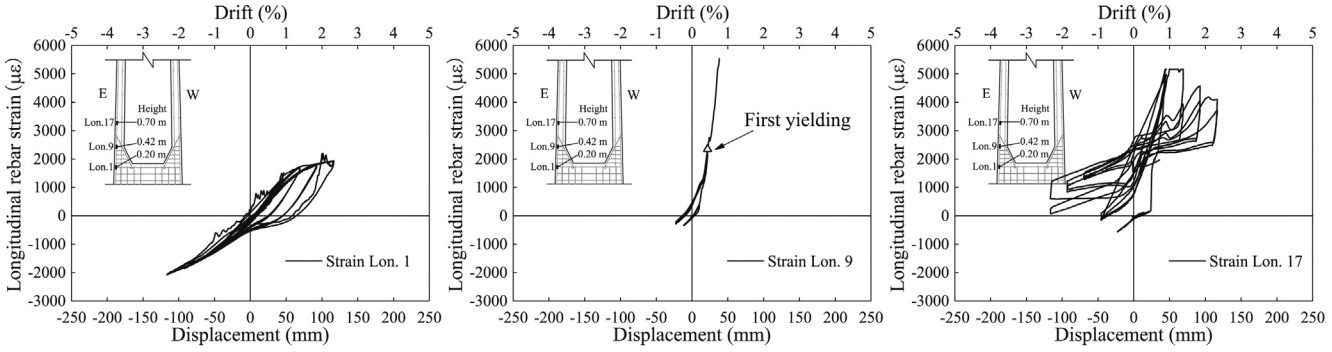

(a) Longitudinal rebar strain in the E face

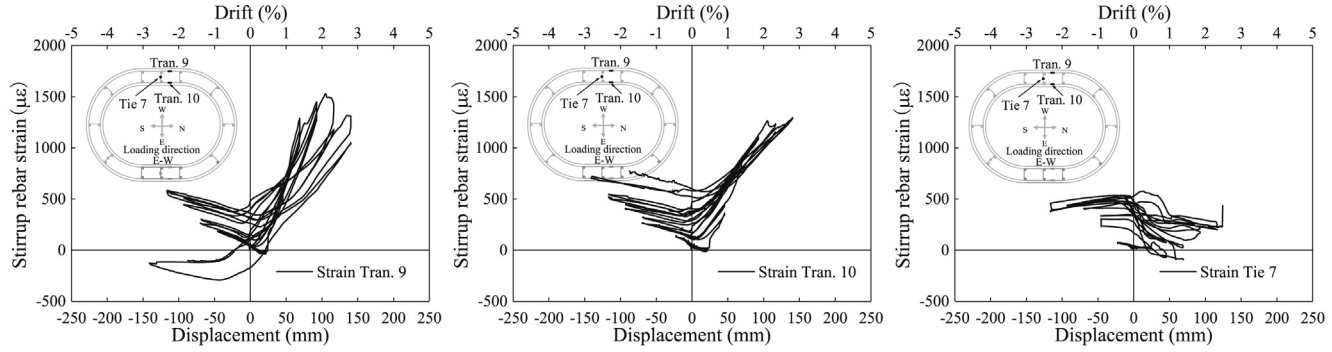

(b) Stirrup rebar strain at a height of 0.70 m

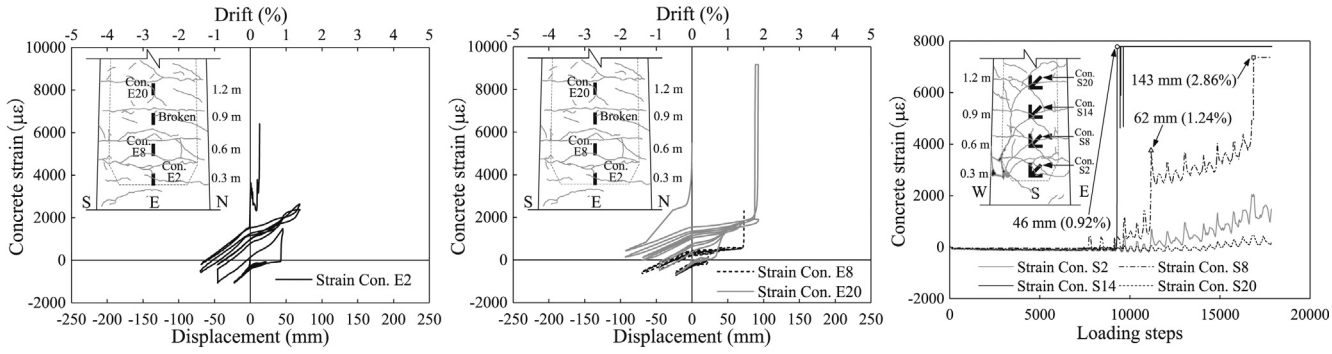

(c) Concrete strain in the E and S faces

Fig. 9. Strain response of specimen SA1.

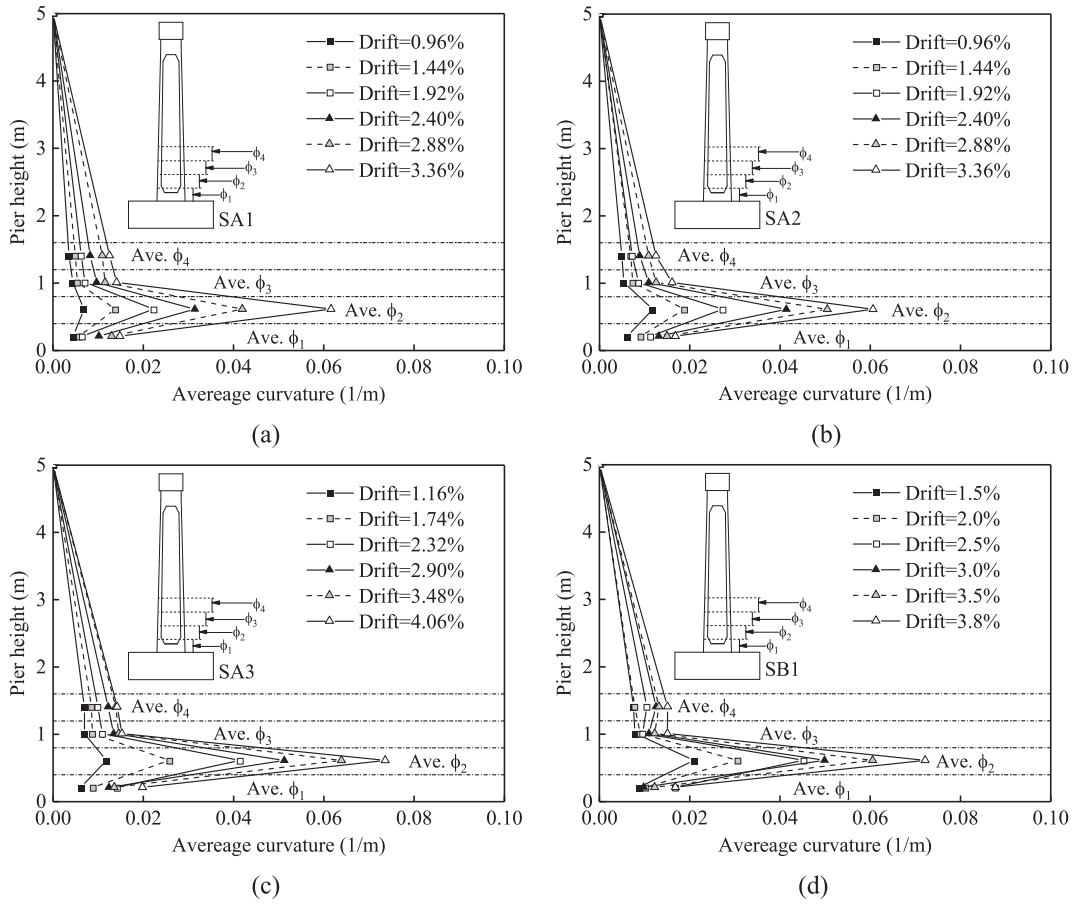

Fig. 10. Distribution of the average curvature: (a) SA1, (b) SA2, (c) SA3, and (d) SB1.

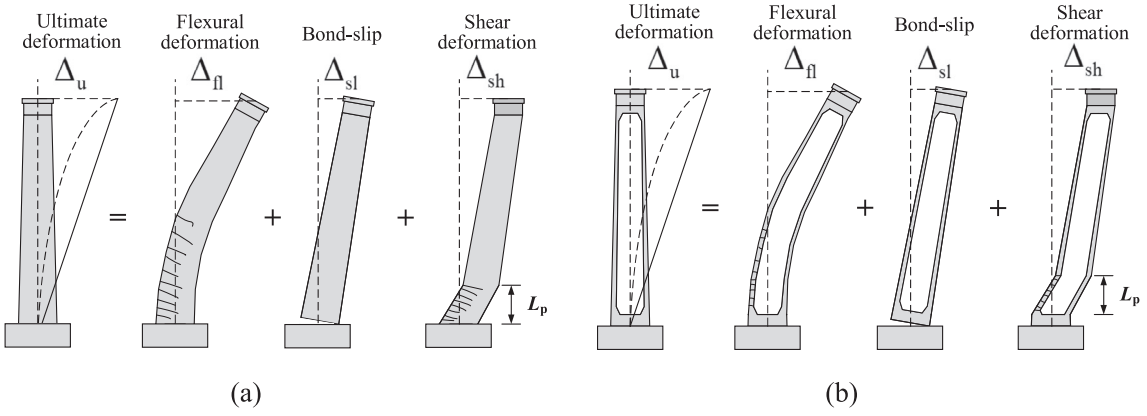

Fig. 11. Deflection of a round-ended pier: (a) solid section, (b) hollow section.

is the average secant stiffness of the *i*th loading cycle, and K_0 is the initial secant stiffness corresponding to the first yielding displacement. The degradation curves of average secant stiffness (K) and factor λ of the specimens are presented in Fig. 15.

It was obvious that the secant stiffness decreased progressively with the increased lateral drift ratio. At the earlier stage of loading course, the secant stiffness decreased quickly, but then the curves became gradually flat. This might attribute to the cracks formed mainly in the earlier loading cycles and weakened the effective area of the section. Conversely, there were few new cracks at the postpeak stage. The residual secant stiffness was approximately 20% of the initial value at the ultimate state. To better describe the characteristics of stiffness, the relationship between the coefficient of stiffness deterioration λ and the displacement ductility factor μ_{Ini} was written as:

$$\lambda = -0.4\ln(\mu_{Ini}) + 1 \tag{3}$$

4.4. Energy dissipation and viscous damping

During the degradation of strength and stiffness along with damage evolution of the piers, the input earthquake energy was dissipated. The dissipated energy was defined as the area of the hysteresis loops, which reflected the capacity to dissipate the earthquake energy through the inelastic hysteretic behavior of the RC members [21]. The dissipation energy in each cycle was shown in Fig. 16a. It showed that the energy dissipation of the specimens, except for SB1, was very close to each

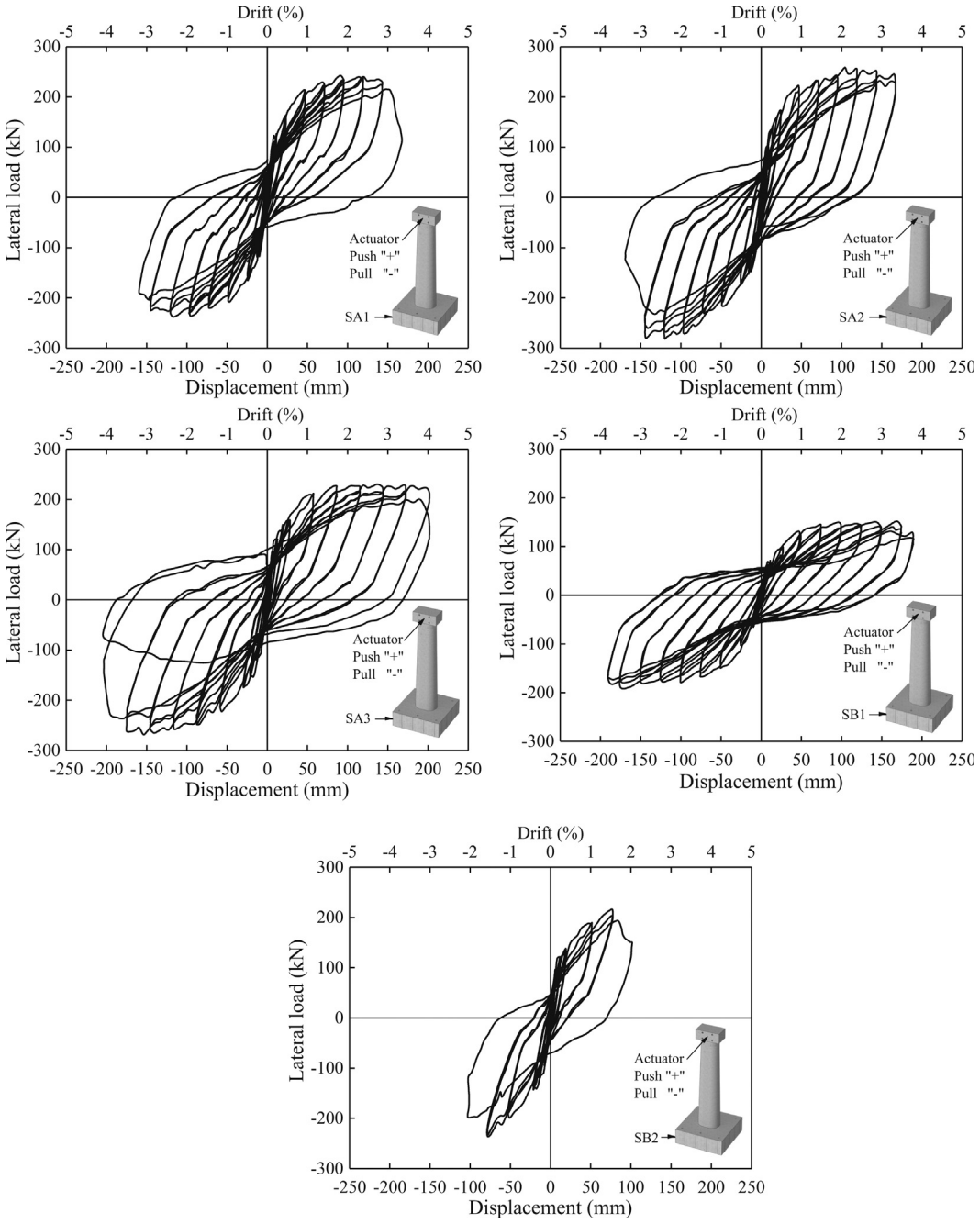

Fig. 12. Hysteresis curves of the specimens.

other. This was reasonable because SB1 was under a comparatively low axial compression with a smaller lateral load. Specimen SA3 was endowed with the largest energy dissipation, which indicated that enhancing stirrups could significantly improve the dissipative capacity of earthquake energy.

The dissipative capacity can be estimated by the equivalent damping ratio ξ_{eq}, which was often adopted in the literature to normalize the dissipated energy [22]. The equivalent viscous damping reflected the combined effects of elastic and hysteretic damping, which was commonly derived from the equation of the energy dissipated in an actual structure and an equivalent viscous system [23]. Usually, the total equivalent viscous damping could be divided into two parts:

$$\xi_{eq} = \xi_0 + \xi_{hyst} \tag{4}$$

where ξ_0 represents the elastic damping and ξ_{hyst} corresponds to the hysteretic damping. The initial damping ratio of concrete is considered to be 5%.

In this study, the equivalent damping ratio $\xi_{eq,i}$ in each cycle could be given as [22]:

$$\xi_{eq,i} = \frac{1}{2\pi} \cdot \frac{E_{d,i}}{(0.5 \cdot V_i^+ \Delta_i^+ + 0.5 \cdot V_i^- \Delta_i^-)} \tag{5}$$

where V_i is the peak load in the ith cycle and Δ_i is the corresponding displacement in both positive and negative direction. $E_{d,i}$ is the energy dissipated in the ith cycle.

In existing literature, several expressions were put forward to calculate the equivalent viscous damping ratio as a function of the displacement ductility. Generally, these models were developed by assuming hysteretic models (e.g., [24]) or regression analysis based on quasi-static test results (e.g., [25]). The comparison of prediction values

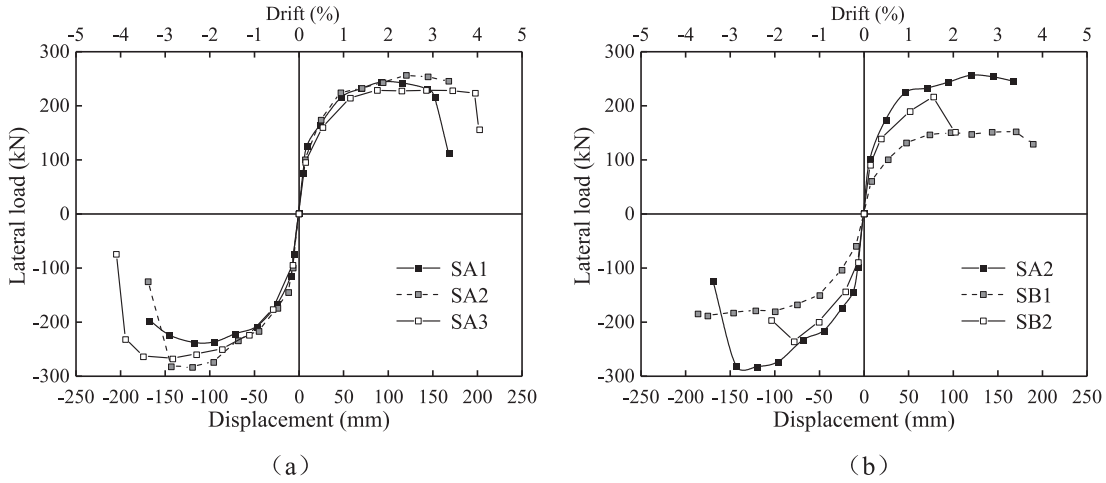

Fig. 13. Skeleton curves: (a) volumetric stirrup ratio; (b) axial compression ratio.

by two typical models with experimental results was shown in Fig. 16b. It was noted that the varying trend of proposed models agreed well with the experimental data, yet some difference existed especially in early loading cycles. Therefore, a regression formula was obtained from the available experimental data as a function of initial displacement ductility $\mu_{Ini,}$ reported in Eq. (6):

$$\xi_{eq} = \begin{cases} 0.005\mu_{Ini} + 0.12 \, (1.0 \leqslant \mu_{Ini} < 3.0) \\ 0.082 \ln \mu_{Ini} + 0.045 \, (\mu_{Ini} \geqslant 3.0) \end{cases} \quad (6)$$

5. Discussion on influencing factors

In this section, the influencing factors on the seismic performance of the round-ended hollow piers were discussed in view of volumetric stirrup ratio, axial compression ratio, and geometry properties.

5.1. Volumetric ratio of stirrup steel

For specimens with stirrup ratios of 0.325% (SA1), 0.910% (SA2) and 1.510% (SA3), it could be found that increasing stirrups exerted slight effect on the strength of specimens but considerably improved the ductile performance of the hollow piers. The extent of plasticity of SA1 was not as obvious as that of SA2 and SA3 arranged with more stirrup. When the ultimate state was reached for specimen SA1, one concrete block even spalled (seen in Fig. 7e and f) with about 2/3 of the space between the adjacent stirrups. As a result, the lower volumetric stirrup ratio with larger hoop spacing resulted in more brittle behavior for round-ended hollow piers. On the contrary, a plastic hinge formed more easily with enhancing stirrup, which was favorable for ductility improvement and hysteretic energy dissipation. This was attributed to the confinement effect of lateral steel, which would considerably delay concrete crushing and reinforcement buckling. The similar positive trend could be also found in degradation curves as observed in Figs. 14 and 15, which greatly improved the residual strength and stiffness of the piers. In short, the volumetric ratio of stirrup reinforcement played a significant role for the round-ended hollow piers when subjected to intensive earthquake.

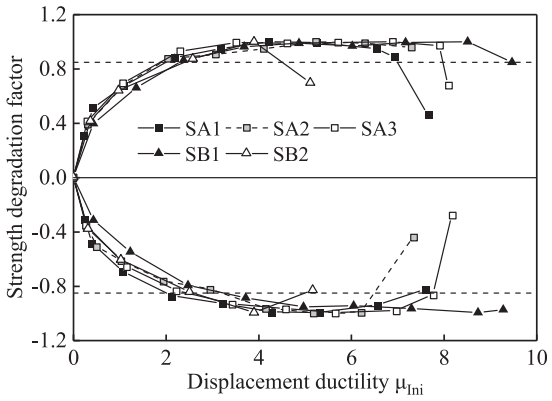

Fig. 14. Strength degradation curves of the specimens.

5.2. Axial compression ratio

According to the test results of the specimens with axial compression ratios of 0.1 (SB1), 0.15 (SA2) and 0.2 (SB2), increasing compression within a moderate range would increase the lateral resistance and stiffness of the specimens. As observed in Fig. 13, it showed that the initial stiffness and the maximum lateral strength increased noticeably with the increasing axial compression. Because moderately higher axial load could effectively enhance the bending capacity for the large-eccentric compressive members. However, excessive axial compression would have harmful effect on plastic behavior, which meant lower ductility (SA2) and even premature crushing of concrete in the

Table 4
Feature points on the skeleton curves.

Specimen	Δ_{yi}/mm	Δ_{ye}/mm		V_{ye}/kN		Δ_m/mm		V_m/kN		Δ_u/mm		V_u/kN		$\mu_{Park} = \Delta_u/\Delta_{ye}$		$\mu_{Ini} = \Delta_u/\Delta_{yi}$	
		N	P	N	P	N	P	N	P	N	P	P	N	P	N	P	N
SA1	22.0	42.7	−38.5	202	−197.2	93	−116.9	243.5	−239.3	154.2	−156.6	206.9	−203.2	3.6	4.1	7.0	7.1
SA2	23.0	43.5	−55	215.5	−225	120.4	−119.3	256	−284	167.9	−151.2	217.6	−241.4	3.9	2.7	7.3	6.6
SA3	25.0	44.6	−53	192.3	−221	142.9	−141.5	229.5	−268.2	199.8	−194.9	195.3	−227.3	4.5	3.7	8.0	7.8
SB1	20.0	47.2	−57.3	130.9	−158.5	170.6	−175.1	151.7	−188.9	189.4	−186	129	−160.6	4.0	3.2	9.5	9.3
SB2	20.0	45.8	−48.1	177.3	−197.2	78.1	−78.1	216.2	−236.5	90.5	−101.7	183.2	−201	2.0	2.1	4.5	5.1

Note: N for positive direction in pushing loading, P for negative direction in pulling loading.

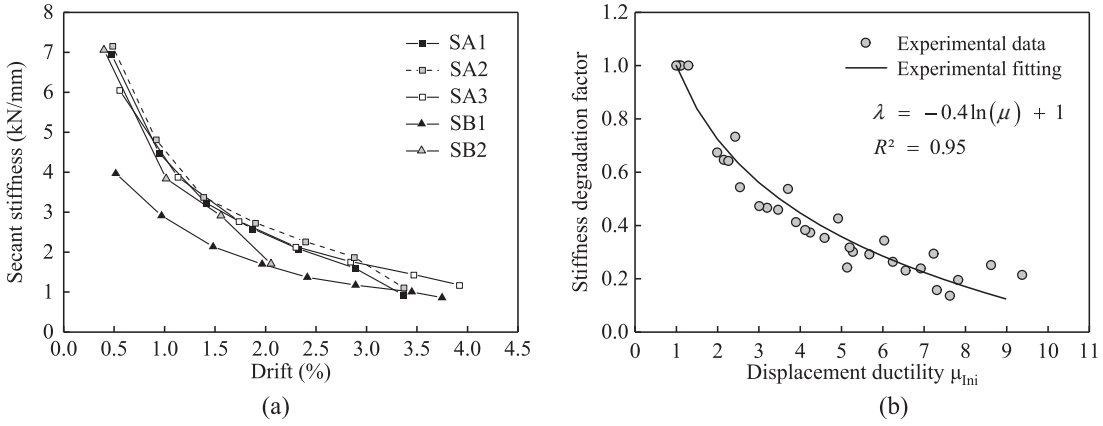

Fig. 15. Degradation curves: (a) secant stiffness *K*; (b) degradation factor λ.

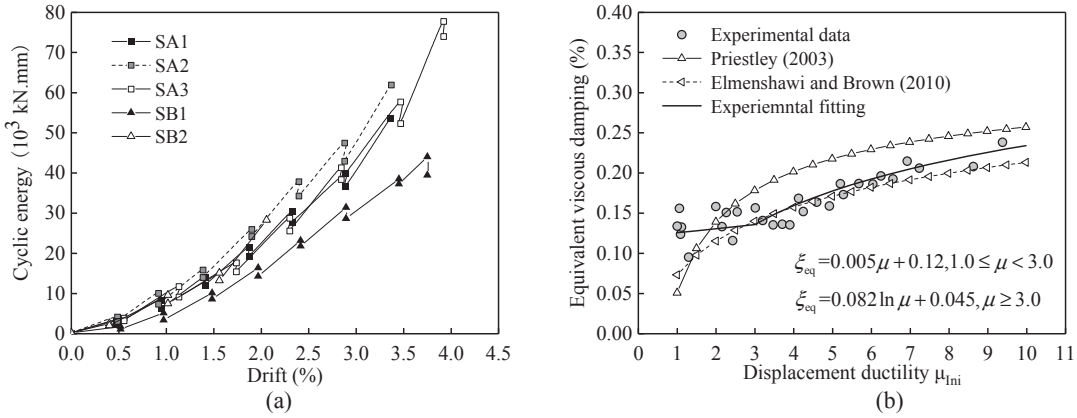

Fig. 16. Energy dissipation (a) and damping ratio (b).

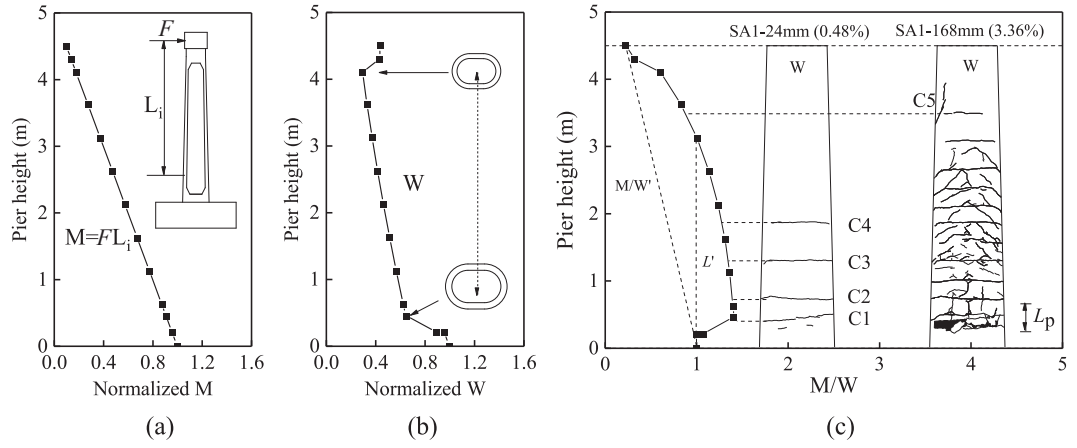

Fig. 17. Distribution of normalized moment (a), modulus (b), and nondimensional stress M/W (c).

weakened region, such as SB2. Therefore, the axial compressive load ratio of the control section (the upper edge of internal chamfer) should be strictly controlled in the seismic design of round-ended hollow piers.

5.3. Geometry details and sectional shape

As the main force-bearing component of bridges, the geometry details and sectional shape have great influence on the seismic performance of round-ended hollow piers. Generally, the round-ended hollow section could be thought of the combination of two thin-walled rectangular and two semicircular, offering enough sectional stiffness for the HSR bridges. Thus, the damage behavior was characterized by rectangular and circular columns to a certain extent [6,12]. However, some original and interesting characteristics were observed in this study. As illustrated in Fig. 17, the nondimensional stress (M/W) along with the normalized moment (M) and sectional modulus (W) were shown respectively. It showed that M distributed linearly along the pier, but W varied considerably at the positions with abrupt-change sections. The maximum M/W was consequently located at the control section with a height of 0.42 m from the base, where the concrete spalled and reinforcement ruptured. The cracks mainly distributed within the scope of *L*' where the fiber stress of the pier was larger than the concrete cracking stress. However, for the uniform-section columns in previous literature, the nondimensional stress distributed linearly in the hollow-

Table 5
Quantification of seismic performance levels.

Level	Performance Level	Qualitative description	Quantitative description	Author	μ_{Park}	μ_{Ini}	γ	λ
I	No	Onset of hairline cracks	Cracks barely visible	Extremely minor cracks	0–0.5	0–1.0	–	1.0
II	Minor	Theoretical first yield of longitudinal bar	Crack widths < 1 mm	Yielding of longitudinal reinforcement	0.5–1.3	1.0–2.5	–	0.63–1.0
				Cracks range from 0.1 to 0.8 mm				
III	Moderate	Initiation of inelastic deformation. Onset of concrete spalling. Development of diagonal cracks	Crack widths 1–2 mm	Cracks range from 0.8 to 2 mm	1.3–2.7	2.5–5.3	–	0.33–0.63
			Length of spalling region > 1/10 cross-section depth	Development of diagonal cracks				
				Initiation of concrete spalling				
				formation of the plastic hinge				
IV	Major	Wide crack widths/spalling over full local region	Crack widths > 2 mm	Crack widths > 2 mm	2.7–3.6	5.3–7.2	0.85–1.0	0.21–0.33
			Diagonal cracks extended over 2/3 cross-section depth	Initiation of strength degradation				
			Length of spalled region > 1/2 cross-section depth	Severe spalling of concrete				
V	Collapse Control	Buckling of main reinforcement. Rupture of lateral bar. Crushing of core concrete	Crack widths > 2 mm in concrete core. Measurable dilation > 5% of original member size	Buckling or fracture of main reinforcement	3.6–4.5	7.2–9.5	0.8–0.85	0.12–0.21
				Crushing of core concrete				
				Lateral load decreases to 85% of peak value				

Note: Given that the specimen SB2 failed owing to premature concrete crushing, the quantification of seismic performance levels was mainly based on the other four piers. Factor γ represented the strength degradation ($\gamma = V_i/V_m$), factor λ represented the stiffness degradation ($\lambda = K_i/K_0$).

section segment, and the maximum stress located at the end of the pier. Due to the influence of solid-section segment, internal chamfer and variable hollow section, the plastic hinge region moved upwards and lengthened to some degree compared with the uniform-section columns [14].

6. Quantification of seismic performance objectives

Unlike novel isolation system (e.g., rocking piers [26]), the inelastic response of RC members as per ductile seismic design was well recognized [5–14]. In the ductile approach, multilevel performance objectives were established under different intensity earthquakes to meet the different requirements of the structures [27]. Usually, the acceptable amount of damage in a bridge under a design earthquake was determined according to its importance, reparability, post-earthquake serviceability etc. For example, moderate damage was permitted in the selected prototype bridges, which could be well repaired or retrofitted via several methods in the post-earthquake rehabilitation [28,29]. However, the definition and quantification of limit states and associated performance were not in consensus among researchers. Therefore, the seismic performance objectives were defined and quantified for the round-ended hollow piers in this section, based on the foregoing damage assessment and analysis of the test results.

It was known that the damage behavior was often associated with the displacement ductility, strength and stiffness degradation. Thus, the ductility was chosen as the quantification factor, along with strength and stiffness degradation factors. Based on the quantification proposed by Hose et al. [30], the seismic performance of round-ended hollow piers was classified into five levels based on the simplified load-displacement curve (also called the performance curve), namely, no damage, minor damage, moderate damage, major damage and collapse control, as shown in Table 5. The nondamage level needed no repair. At the minor damage level, the bridge could be immediately opened to traffic while rehabilitation was required for the durable service. Under the moderate damage state, emergency traffic could be allowed after quick inspection, and considerable repair work was needed. At the major damage level, emergency traffic could be permitted yet rehabilitation might be infeasible due to severe damage or residual drift. In the final level, seismic safety was guaranteed but rebuilding was needed. It could be found that the round-ended hollow piers were under moderate damage state when the ductility μ_{Ini} was the allowable limitation of 4.8 in the current seismic code of railway engineering of China [15].

7. Conclusions

In this study, five 1/6-scale round-ended hollow pier specimens were designed, built, and tested under semi-static cyclic loading. The crack patterns, failure modes, strain responses, plastic behavior and quantification of performance level were studied. Analysis of the investigation was performed in terms of hysteretic response, ductility, load carrying capacity, stiffness degradation, energy dissipation, and viscous damping. The key parameters affecting the seismic performance of round-ended hollow piers were discussed, including volumetric stirrup ratio, axial compression level, geometry details, cross sectional shape. Finally, the seismic performance objectives were quantified for the round-ended hollow piers. Based on the test results above, the main conclusions were summarized as follows:

(1) All the specimens suffered flexure-type failure with plump hysteresis curves. The damage region focused around the internal chamfer and nearby hollow segment where concrete squashed and longitudinal rebar buckled or ruptured. The flexural crack distribution covered around two-thirds of the pier height.
(2) The plastic hinge region moved upwards and lengthened owing to the existence of solid segment, internal chamfer and variable

hollow section. Meanwhile, the crossed diagonal cracks on the pier side-faces in plastic region indicated weakened shear capacity of this type of piers. Thus, both flexural and shear capacity of round-ended hollow columns should be guaranteed in damage-prone region, to prevent the members from brittle failure.

(3) Increasing stirrup ratio was helpful to upgrade the displacement ductility and formation of the plastic region. The cumulative energy dissipation of specimen SA3 with the biggest stirrup ratio was better than that of SA1 and SA2. As a result, the volumetric stirrup ratio was better designed no lower than 0.91% for this kind of piers in earthquake-prone area.

(4) Increasing axial compression within a certain range could considerably enhance the initial stiffness and flexural loading capacity. However, an excessive axial compression could decrease displacement ductility due to premature crushing of concrete.

(5) The round-ended hollow piers corresponded to medium damage state at a ductile ratio limitation ($\mu_{Ini} = 4.8$) in the current seismic code of railway engineering of China. This indicated the good performance and sufficient seismic safety of the piers under intensive earthquake.

(6) Due to the limited number of specimens and displacement sensors, further experiment may be conducted to study the plastic hinge behavior of round-ended hollow piers in depth in the future.

Acknowledgments

The financial support provided by the National Natural Science Fund Committee of China (Grant No. 51178395) and the Key Project of Applied Basic Research Plan (Grant No. 2017JY0059) are acknowledged gratefully.

References:

[1] Yan B, Dai GL, Hu N, et al. Recent development of design and construction of short span high-speed railway bridges in China. Eng Struct 2015;100:707–17.
[2] He XH, Wu T, Zou YF, et al. Recent developments of high-speed railway bridges in China. Struct Infrastruct Eng 2017;13(12):1584–95.
[3] Shao CJ. Comprehensive seismic test on railway piers in intensive earthquake zone: experimental investigation on the seismic performance of railway high piers (report for quasi-static test). Chengdu: Southwest Jiaotong University; 2018. [in Chinese].
[4] Hui Chen. The design of bridge piers with rounded rectangular cross-section in railway 2009;vol. 4:77–9. [in Chinese].
[5] Mander JB, Priestley MJN, Park R. Behavior of ductile hollow reinforced concrete piers. Bull New Zealand Natl Soc Earthq Eng 1983;16(4):273–90.
[6] Yeh YK, Mo YL, Yang CY. Seismic performance of rectangular hollow bridge columns. J Struct Eng 2002;128(1):60–8.
[7] Mo YL, Wong DC, Maekawa K. Seismic performance of hollow bridge columns. ACI Struct J 2003;100(3):337–49.
[8] Yeh YK, Mo YL, Yang CY. Full-scale tests on rectangular hollow bridge piers. Mater Struct RILEM 2002;35:117–25.
[9] Zong ZH, Chen SH, Xia ZH. Bi-axial quasi-static testing research of high hollow reinforced concrete piers. J Dis Prevent Mitigat Eng 2010;30(4):369–74. [in Chinese].
[10] Han Q, Du XL, Zhou YH, et al. Experimental study of hollow rectangular bridge column performance under vertical and cyclically bilateral loads. Earthq Eng Eng Vibrat 2013;12(3):433–45.
[11] Zahn FA, Park R, Priestley MJN. Flexural strength and ductility of circular hollow reinforced concrete piers without confinement on inside face. ACI Struct J 1990;87(2):156–66.
[12] Yeh YK, Mo YL, Yang CY. Seismic performance of hollow circular bridge piers. ACI Struct J 2001;98(6):862–71.
[13] Liu L. Research on seismic design and seismic isolation and reduction control of high-pier and long-span railway bridges. Beijing: Beijing Jiaotong University; 2004. [in Chinese].
[14] Jiang LZ, Shao GQ, Wang H, et al. Experimental study on seismic performance of hollow piers with rounded rectangular cross section in high-speed railways. Eng Mech 2014;31(3):72–82. [in Chinese].
[15] GB 50111-2006 (2009). Code for Seismic Design of Railway Engineering. Beijing (China): Ministry of Housing and Urban-Rural Development of China; 2009 [in Chinese].
[16] Caltrans-2013. Caltrans Seismic Design Criteria [S]. Version 1.7. Sacramento: California Department of Transportation; 2013.
[17] JGJ101-1996 Specification of testing methods for earthquake resistant building. Beijing: China Architecture & Building Press; 1996 [in Chinese].
[18] Jiang LZ, Shao GQ, Jiang J, et al. Experimental study on seismic performance of solid piers with rounded cross-section in high-speed railway. China Civ Eng J 2013;46(3):86–95. [in Chinese].
[19] Megalooikonomou KG, Tastani SP, Pantazopoulou SJ. Effect of yield penetration on column plastic hinge length. Eng Struct 2018;156:161–74.
[20] Park R. Evaluation of ductility of structures and structural assemblages from laboratory testing. Bull New Zealand Natl Soc Earthq Eng 1989;22(3):155–66.
[21] Rodrigues H, Varum H, Arêde A, et al. A comparative analysis of energy dissipation and equivalent viscous damping of RC columns subjected to uniaxial and biaxial loading. Eng Struct 2012;35:149–64.
[22] Cassese P, Ricci P, Verderame GM. Experimental study on the seismic performance of existing reinforced concrete bridge piers with hollow rectangular section. Eng Struct 2017;144:88–106.
[23] Chopra AK. Dynamics of structures. Prentice Hall; 2006.
[24] Blandon CA, Priestley MJN. Equivalent viscous damping equations for direction displacement based design. J Earthq Eng 2005;9:257–78.
[25] Elmenshawi A, Brown T. Hysteretic energy and damping capacity of flexural elements constructed with different concrete strengths. Eng Struct 2010;32:297–305.
[26] Chen YH, Liao WH, Lee CL, et al. Seismic isolation of viaduct piers by means of a rocking mechanism. Earthq Eng Struct Dyn 2006;35:713–36.
[27] Guan ZG, Zhang JH, Li JZ. Multilevel performance classifications of tall RC bridge columns toward postearthquake rehabilitation requirements. J Bridge Eng 2017;22(10). 04017080(1–12).
[28] He R, Grelle S, Sneed LH, et al. Rapid repair of a severely damaged RC column having fractured bars using externally bonded CFRP. Compos Struct 2013;101:225–42.
[29] Truong GT, Kim JC, Choi K. Seismic performance of reinforced concrete columns retrofitted by various methods. Eng Struct 2017;134:217–35.
[30] Hose YD, Silva P, Seible F. Development of a performance evaluation database for concrete bridge components and systems under simulated seismic loads. Earthq Spectra 2000;16(2):413–44.